


Nanoscale Magnetism Probed in a Matter-Wave Interferometer

Yaakov Y. Fein^{1,*}, Sebastian Pedalino^{1,2}, Armin Shayeghi¹, Filip Kiałka¹, Stefan Gerlich¹, and Markus Arndt¹

¹University of Vienna, Faculty of Physics, Vienna Center for Quantum Science and Technology (VCQ), Boltzmannngasse 5, A-1090 Vienna, Austria

²University of Vienna, Vienna Doctoral School in Physics, Boltzmannngasse 5, A-1090 Vienna, Austria

 (Received 16 March 2022; revised 13 May 2022; accepted 7 July 2022; published 12 September 2022)

We explore a wide range of fundamental magnetic phenomena by measuring the dephasing of matter-wave interference fringes upon application of a variable magnetic gradient. The versatility of our interferometric Stern-Gerlach technique enables us to study the magnetic properties of alkali atoms, organic radicals, and fullerenes in the same device, with magnetic moments ranging from a Bohr magneton to less than a nuclear magneton. We find evidence for magnetization of a supersonic beam of organic radicals and, most notably, observe a strong magnetic response of a thermal C₆₀ beam consistent with high-temperature atomlike deflection of rotational magnetic moments.

DOI: [10.1103/PhysRevLett.129.123001](https://doi.org/10.1103/PhysRevLett.129.123001)

Introduction.—Magnetism, from the quantized deflection of atoms in the Stern-Gerlach experiment [1] to bulk ferromagnetism [2], is quantum mechanical at heart. This relationship is symbiotic: Magnetic phase shifts in neutron interferometry were essential in demonstrating a number of fundamental quantum phenomena [3–6], and magnetic gradients have been employed as coherent beam splitters in matter-wave interferometry [7].

Here, we use matter-wave interferometry to measure the magnetic properties of the interfering particles themselves. We apply tunable magnetic gradients within the Long-baseline Universal Matter-wave Interferometer (LUMI) [8,9] and monitor the response of the interference fringes. Unlike in classical beam deflectometry, where one measures the deflection and/or broadening of a macroscopic beam profile, the presence of nanoscale interference fringes allows us to resolve nanometer-level deflections and forces as small as 10^{-26} N [10]. While measuring the envelope phase shift of the fringes is suitable for induced dipole moments [11], monitoring the fringe visibility enables us to study species with permanent dipole moments with relaxed phase stability requirements.

In a three-grating Talbot-Lau interferometer like LUMI [12], a near-field interference pattern is imprinted into the molecular beam density behind the second grating. This takes the form of a near-sinusoidal modulation with periodicity d if the gratings are separated by near multiples of the Talbot length $L_T = d^2/\lambda_{dB}$, with λ_{dB} the de Broglie

wavelength and d the grating periodicity. Transversely scanning the third grating while monitoring the transmitted flux reveals the interference fringes. Talbot-Lau interferometry is a robust technique with good mass scalability and lenient coherence requirements [13], making it particularly attractive for the measurement of molecular properties.

The universality of the interferometry scheme enables us to study a variety of species with vastly different magnetic properties, from alkali atoms to organic molecules. In the case of atoms, visibility modulation upon application of a magnetic gradient is due to the dephasing and rephasing of the atomic hyperfine substates in the unpolarized beam, similar to previous atom interferometry experiments [14–16]. The magnetic phase accumulation for isolated molecules is more subtle due to additional degrees of freedom such as vibrational and rotational modes. At low vibrational temperatures, spins can be locked to a molecular axis [17], while internal spin relaxation [18] and avoided crossings in the Zeeman manifold due to spin-rotation coupling [19] can lead to Langevin-like paramagnetism and one-sided deflection in a magnetic gradient. Such effects complicate the interpretation of molecular Stern-Gerlach experiments [20], but at the same time provide access to the richer physics of molecular magnetism.

The key features of our setup are sketched in Fig. 1. Knudsen cells were used to produce thermal atomic and fullerene beams, while a pulsed valve was used to create a supersonic beam of organic radicals. The interferometer consists of three gratings of period $d = 266$ nm equidistantly spaced by $L = 0.98$ m. Three nanomechanical gratings were used for the atomic experiments, while an optical phase grating formed by a retroreflected 532 nm laser beam was used as the central grating for the molecules [21].

Published by the American Physical Society under the terms of the [Creative Commons Attribution 4.0 International license](https://creativecommons.org/licenses/by/4.0/). Further distribution of this work must maintain attribution to the author(s) and the published article's title, journal citation, and DOI.

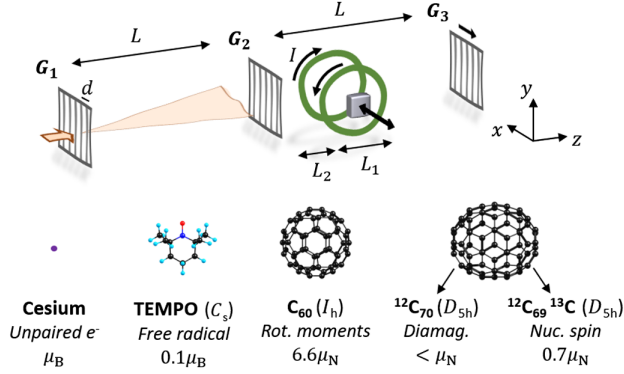


FIG. 1. The interferometer with three equidistantly spaced gratings G_{1-3} and the magnetic interaction region between G_2 and G_3 . The latter consists of an anti-Helmholtz coil pair for the atomic experiments and a permanent magnet for the molecular experiments. G_3 is scanned along the x axis to mask the sinusoidal interference fringes before mass selection and detection of the transmitted flux. The studied species are shown with their corresponding point groups, the origin of their dominant magnetism observed in our scheme, and typical magnitudes of the associated magnetic moments.

We apply magnetic gradients across the molecular beam to yield a differential magnetic phase shift for the interferometer paths. For the atomic experiments, we employed anti-Helmholtz coils similar to Refs. [15,16]. The zero-field region at the coil center was avoided by 8 mm to prevent nonadiabatic spin flips. For the molecular experiments, we required stronger magnetic gradients, so we instead used a permanent rare-earth magnet that could be translated transversely to the molecular beam. The lengths $L_{1,2}$ defined in Fig. 1 extend beyond the physical extent of the coils or permanent magnet, taking fringe fields into account (see Supplemental Material [22]). Characterizations of the magnetic fields as well as the modeled field gradients for both the coils and the permanent magnet are provided in the Supplemental Material [22]. We find good agreement with theoretical models for both systems [31,32].

Atomic theory.—Atoms with nonzero spin exhibit Zeeman splitting in a magnetic field B , and an atomic beam is thus symmetrically deflected in a magnetic gradient [1]. Our atomic experiments are conducted in the weak-field regime ($B < 100$ G), and are therefore sensitive to the hyperfine structure rather than merely the electronic spin. We can write the semiclassical force on a given hyperfine substate m_F as

$$\mathbf{F} = -\nabla(-\boldsymbol{\mu} \cdot \mathbf{B}) = m_F g_F \mu_B \nabla B, \quad (1)$$

with $B = |\mathbf{B}|$, $\boldsymbol{\mu}$ the magnetic moment, g_F the Landé g factor, and μ_B the Bohr magneton. Here we have implicitly assumed adiabatic following of $\boldsymbol{\mu}$ along \mathbf{B} . The transverse component of the force yields an envelope phase shift of the interference fringes [33]. For a given longitudinal

velocity v and substate m_F , this phase shift is (see also Supplemental Material [22])

$$\phi_{m_F} = \frac{2\pi m_F g_F \mu_B}{d m v^2} C \quad (2)$$

with

$$C = \int_0^{L_1} \int_0^z \frac{\partial B}{\partial x} dz' dz + L_{\text{drift}} \int_0^{L_1} \frac{\partial B}{\partial x} dz. \quad (3)$$

Here, $L_{\text{drift}} = L - L_1 - L_2$, and B in general contains a small constant (i.e., not current-dependent) contribution due to background fields. The first term corresponds to the deflection within the force region, while the second term accounts for the displacement that accumulates over the remaining drift length, assuming a constant forward velocity. For the anti-Helmholtz coils, we find $C = 10.3$ Gm for a current of 1 A.

The measured interference pattern is the sum of the N individual hyperfine interference patterns averaged over the velocity distribution $\rho(v)$. Considering the symmetry of the $\pm m_F$ deflections, the visibility V can be written as

$$V = \frac{V_0}{N} \left| \int_0^\infty \rho(v) A(v) \sum_{F, m_F} \cos[\phi_{m_F}(v)] dv \right|. \quad (4)$$

Here, V_0 is the maximum visibility in the absence of magnetic gradients, and $A(v)$ is a weak dependence of the visibility amplitude on velocity [34], which we neglect for the atomic and radical experiments. The hyperfine structures of the studied isotopes are provided in the Supplemental Material [22].

Cesium results.—In Fig. 2, we show the interference visibility of ^{133}Cs as a function of the anti-Helmholtz coil current for two different velocity distributions. To a good approximation, all magnetic substates m_F are equally populated in the thermal atomic beam. As the magnetic gradient is increased, the visibility decreases as the interference fringes of the various hyperfine states are interspersed, until a value at which each pair of hyperfine substates $\pm m_F$ is mutually deflected by a multiple of d , at which point the patterns overlap and the visibility revives. The broad velocity distribution washes out these revivals, leaving an asymptote corresponding to the number of nonmagnetic ($m_F = 0$) substates divided by the total number of hyperfine substates N (2/16 for ^{133}Cs).

There is good agreement between the data and Eq. (4) when we include a fitted constant offset to C of 0.4 Gm, which we attribute to background field gradients (see Supplemental Material [22]). The deviation from theory at currents below 0.15 A is consistent with residual magnetic fields along the flight path, while the drop at currents above 4.5 A is likely nonmagnetic in origin.

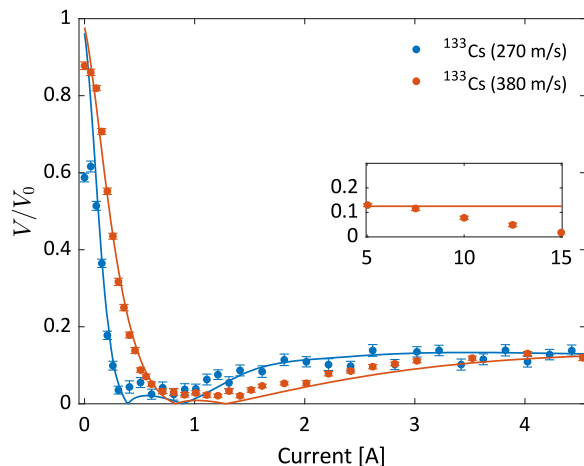


FIG. 2. Cesium interference visibility as a function of the anti-Helmholtz coil current. The solid curves are obtained from Eq. (4), where we fit a small constant offset to the calculated C factor. The inset shows the high-current behavior, with the line indicating the expected asymptote. Each point consists of multiple interference scans, and error bars are standard errors. Visibilities are normalized using the asymptotic value rather than the zero-current point (see Supplemental Material [22]).

See the Supplemental Material [22] for further details as well as additional rubidium data.

Molecular theory.—For atoms and molecules with neither nuclear nor electronic spin, strong magnetic gradients can still yield observable deflections [10,35,36] due to induced magnetic moments $\boldsymbol{\mu} = m\chi_m\mathbf{B}/\mu_0$, with m the particle mass and χ_m the mass susceptibility. The resulting, typically diamagnetic [2], deflection of the interference pattern is one-sided, causing visibility loss with increasing $(\mathbf{B} \cdot \nabla)B_x$ due to the finite velocity spread [9,10].

Molecular beam dynamics are richer than for atomic beams, since there are typically a number of excited molecular body rotations with corresponding rotational magnetic moments $\boldsymbol{\mu}_{\text{rot}}$. For molecules with both spin and rotational angular momentum in an external magnetic field, one must consider spin-rotation coupling in addition to the usual Zeeman interaction terms [37]. The resulting Zeeman splitting thus depends on whether B is strong enough to decouple spin and rotation or if a coupled basis is more appropriate. Since the rotational g factor (g_{rot}) is typically much smaller than the spin g factor (g_{spin}), the Zeeman splitting is usually dominated by spin in the strong-field regime of the molecular experiments [20].

Stern-Gerlach experiments on polyatomic species with spin and rotational degrees of freedom can exhibit one-sided rather than symmetric deflection as obtained for atoms. This has been observed in metal cluster beams [38–40], which exhibit a time-averaged projection of the magnetic moment onto the magnetic field axis of the form $\mu_{\text{eff}} \propto \mu^2 B/k_B T$. This corresponds to the low-field and high-temperature limit of the Langevin function, typically

associated with bulk paramagnetism [41]. In molecular beams, the numerical prefactor of μ_{eff} and the relevant temperature depend on whether the spin is locked to the molecular framework or can thermally fluctuate [17,42]. The origin of magnetization in an isolated molecular system has been the subject of debate and has been explained via both a superparamagnetic model [18,42,43] and an avoided crossing model arising from spin-rotation coupling [19,44,45].

The response of molecular interference fringes to a magnetic gradient depends on whether the deflection is symmetric or one-sided. For atomlike symmetric deflection, the theory is analogous to Eq. (4), while for one-sided deflection one expects monotonic visibility loss due to averaging over the velocity distribution given by

$$V = V_0 \left| \int_0^\infty \rho(v)A(v) \exp[i\phi(v)]dv \right|, \quad (5)$$

where $\phi \propto \mu_{\text{eff}}$ for magnetized molecules or $\phi \propto \chi_m B$ for a diamagnetic response.

Organic radical results.—The organic radical TEMPO [(2,2,6,6-Tetramethylpiperidin-1-yl)oxyl] is used as a spin label in electron spin resonance spectroscopy and has also been studied in Stern-Gerlach experiments [46,47]. A molecular beam was formed by supersonic expansion from a pulsed valve [48] (see Supplemental Material [22]) with a Gaussian velocity distribution centered at 694 m/s and a spread of only 23 m/s. The response of TEMPO interference fringes to the permanent magnet is shown in Fig. 3. Analogous experiments with the TEMPO dimer indicated qualitatively similar behavior, albeit with poorer statistics due to the lower beam flux.

While a quantitative understanding of the magnetic response requires knowledge of the spin-rotation coupling in the system, we consider two simplified regimes. The dashed line shows a symmetric deflection model in which the response is determined exclusively by the unpaired electron in the strong-field regime (since $g_{\text{spin}} \gg g_{\text{rot}}$; see earlier discussion). The dotted line instead assumes one-sided deflection due to Langevin-like spin alignment in the locked-moment regime [17], where we have used $T_{\text{rot}} = 10$ K (a typical value for such supersonic expansions [49]) and approximated the molecule as a prolate symmetric top (see Supplemental Material [22]). Both the damping of the oscillations in the symmetric deflection model and the visibility loss of the one-sided deflection model are due to the velocity spread of the beam.

The observed response lies between these regimes: The solid line shows a one-sided deflection model assuming an effective magnetic moment of $\mu_{\text{eff}} = 0.1 \mu_B$ in Eq. (5). Such an intermediate response could be due to TEMPO exhibiting a degree of Langevin-like magnetization (potentially due to spin-rotation coupling [19,44]) as well as residual symmetric deflection [45]. This is consistent with

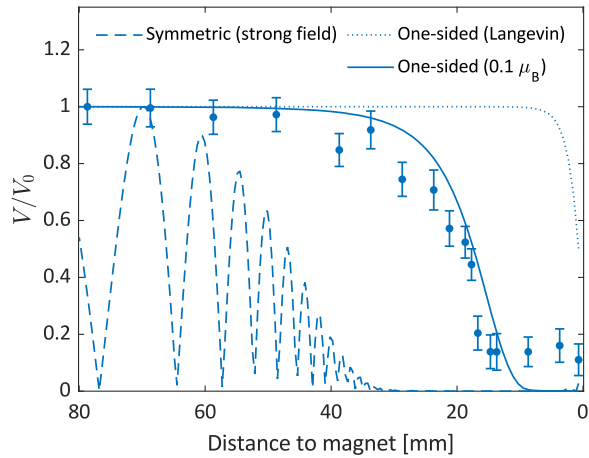


FIG. 3. TEMPO interference visibility as a function of the magnet distance. We consider three models: a symmetric deflection model of the unpaired electronic spin (dashed line), a one-sided deflection model assuming a purely Langevin-like response at 10 K (dotted line), and a one-sided deflection model assuming $\mu_{\text{eff}} = 0.1 \mu_B$ (solid line). The nonzero baseline of the data is likely a fitting artifact, also seen for the C_{60} isotopomers in the Supplemental Material [22]. Visibilities are normalized to the first data point (magnet withdrawn) and error bars are standard errors.

previous experiments [47], in which indications of asymmetric splitting were tentatively attributed to an avoided crossing model.

Fullerene results.—The response of C_{60} and C_{70} interference visibility to the permanent magnet is shown in Fig. 4. The weakly diamagnetic nature of these fullerenes in bulk is well established [50]. The $^{12}C_{70}$ response agrees well with the predicted visibility loss due to one-sided diamagnetic deflection. The theory curve has no free parameters, using only the literature diamagnetic susceptibility value of C_{70} and the empirical velocity distribution. An observed phase shift of the interference fringes away from the magnet further confirms the expected diamagnetic response. The magnitude of the diamagnetically induced magnetic moment near the surface of the magnet is calculated to be $\approx 0.4 \mu_N$, with μ_N the nuclear magneton.

With its unpaired nuclear spin, $^{12}C_{69}^{13}C$ exhibits a more rapid loss of fringe visibility than $^{12}C_{70}$. The behavior can be described by symmetric deflection of the ^{13}C magnetic moment (together with the one-sided diamagnetic deflection), assuming a strong-field response dominated by the nuclear spin. The stronger response of $^{12}C_{69}^{13}C$ compared to $^{12}C_{70}$ implies an absence of Langevin-like magnetization, which would predict complete relaxation of the nuclear spin (since $k_B T \gg \mu_B$).

The most surprising finding in this measurement series was the strong magnetic response of C_{60} , as seen for all isotopomers (see Supplemental Material [22]). With no electronic spin or orbital angular momentum (or even nuclear, in

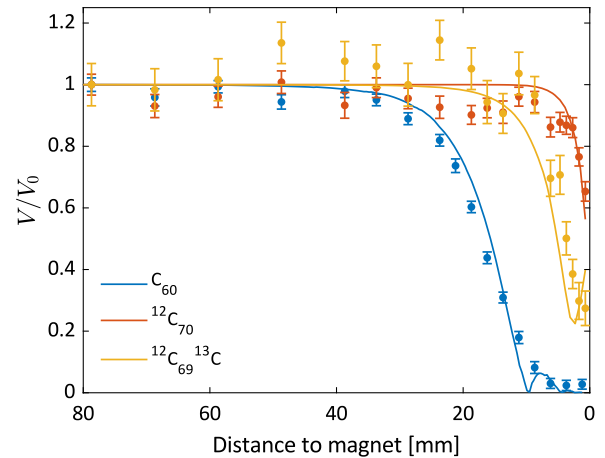


FIG. 4. C_{60} (all isotopomers), $^{12}C_{70}$ and $^{12}C_{69}^{13}C$ interference visibility as a function of the magnet distance. There are three distinct magnetic phenomena on display here: one-sided diamagnetic deflection of $^{12}C_{70}$, symmetric deflection of the nuclear spin of $^{12}C_{69}^{13}C$, and symmetric deflection of rotational moments of C_{60} . Visibilities are normalized to the first data point (magnet withdrawn) and error bars are standard errors. There are no free parameters in the theory curves.

the case of $^{12}C_{60}$), we expected to observe an even weaker diamagnetic response than $^{12}C_{70}$. Instead, we observed a visibility drop which would imply a susceptibility 2 orders of magnitude larger than the literature diamagnetic value.

Since the visibility is completely washed out at high fields, the underlying mechanism must apply to the majority of C_{60} molecules in the beam, ruling out rare transient events like triplet excitation in the optical grating. We also ruled out the possibility that deformed cage structures could have led to dangling bonds [51] by measuring a single NMR peak at 142.8 ppm for both unsublimated and sublimated C_{60} samples. Langevin-like magnetization should play no role here in the absence of spin-rotation coupling [44].

Instead, we attribute the behavior to the symmetric deflection of rotational magnetic moments. The rotational moment of a spherical top molecule is given by $\mu_{\text{rot}} = g_{\text{rot}} \mu_N \mathbf{J}$, with \mathbf{J} the rotational angular momentum [52]. We calculate g_{rot} with density functional theory at the B3LYP/def2-QZVPP level of theory [53,54] using the GAUSSIAN 16 program [55] (see Supplemental Material [22]). We find an isotropic value of $g_{\text{rot}} = -0.0141$ (μ_N units), which, for the most-occupied rotational state $J_{\text{max}} = 466$ [56], gives a maximum projection onto the magnetic field axis of $6.6 \mu_N$.

C_{60} thus behaves as an atom in a high spin state, with the substitution $m_F g_F \mu_B \rightarrow M g_{\text{rot}} \mu_N$, with M the quantum number for the projection of \mathbf{J} onto \mathbf{B} . The visibility response can be calculated using Eq. (4), replacing the summation over F , m_F with an integration over M from $-J_{\text{max}}$ to J_{max} [57]. This gives the solid theory curve in Fig. 4, which agrees well with the measured response.

To understand why C_{70} shows no comparably strong effect of rotational moments ($^{12}C_{70}$ is consistent with a diamagnetic response alone), one must consider the difference in molecular symmetry. For a prolate symmetric top like C_{70} , there is the additional projection of \mathbf{J} onto the molecular symmetry axis given by the quantum number K . The ensemble average over K combined with the small g_{rot} values of C_{70} (see Supplemental Material [22]) reduces the magnitude of the effect [58]. Moreover, the small g_{rot} values mean that the timescales of precession and magnetic field change become comparable, leading to a breakdown of adiabatic following and a reduced role of rotational moments in the case of C_{70} (see Supplemental Material [22]).

Conclusion.—Our interferometric Stern-Gerlach technique offers significantly improved spatial and force resolution compared to classical beam deflectometry and enables us to measure magnetic effects spanning orders of magnitude in strength in the same device. We have observed the symmetric splitting of alkali atoms, the magnetization of an organic radical beam, and the weak one-sided diamagnetic deflection of C_{70} . Most intriguingly, we have observed a strong magnetic response of C_{60} , which in bulk is even less diamagnetic than C_{70} . The magnetic response is consistent with atomlike deflection of rotational magnetic moments. Particularly noteworthy is the emergence of this quantized behavior at high rotational temperatures, where the classical limit is typically reached.

We would like to acknowledge the experimental assistance of Tomás Sousa, Philipp Geyer, and Richard Ferstl as well as the University of Vienna NMR Center for the C_{60} analysis. This project has received funding from the European Research Council under the European Union’s Horizon 2020 Research and Innovation Program (Grant No. 320694), and the Austrian Science Fund within Programs No. P-30176, No. W-1210-N25, and No. P-32543-N. The computational results presented were obtained using the Vienna Scientific Cluster within Grant No. 70918.

* yaakov.fein@univie.ac.at

- [1] W. Gerlach and O. Stern, Der experimentelle Nachweis des magnetischen Moments des Silberatoms, *Z. Phys.* **8**, 110 (1922).
- [2] J. H. Van Vleck, *The Theory of Electric and Magnetic Susceptibilities* (Oxford University Press, New York, 1932).
- [3] B. E. Allman, A. Cimmino, A. G. Klein, G. I. Opat, H. Kaiser, and S. A. Werner, Observation of the scalar Aharonov-Bohm effect by neutron interferometry, *Phys. Rev. A* **48**, 1799 (1993).
- [4] A. G. Wagh, V. C. Rakhecha, J. Summhammer, G. Badurek, H. Weinfurter, B. E. Allman, H. Kaiser, K. Hamacher, D. L. Jacobson, and S. A. Werner, Experimental Separation of Geometric and Dynamical Phases Using Neutron Interferometry, *Phys. Rev. Lett.* **78**, 755 (1997).
- [5] H. Rauch, A. Zeilinger, G. Badurek, A. Wilfing, W. Bauspiess, and U. Bonse, Verification of coherent spinor rotation of fermions, *Phys. Lett.* **54A**, 425 (1975).
- [6] S. A. Werner, R. Colella, A. W. Overhauser, and C. F. Eagen, Observation of the Phase Shift of a Neutron due to Precession in a Magnetic Field, *Phys. Rev. Lett.* **35**, 1053 (1975).
- [7] S. Machluf, Y. Japha, and R. Folman, Coherent Stern-Gerlach momentum splitting on an atom chip, *Nat. Commun.* **4**, 2424 (2013).
- [8] Y. Y. Fein, P. Geyer, P. Zwick, F. Kiařka, S. Pedalino, M. Mayor, S. Gerlich, and M. Arndt, Quantum superposition of molecules beyond 25 kDa, *Nat. Phys.* **15**, 1242 (2019).
- [9] Y. Y. Fein, Long-baseline universal matter-wave interferometry, Ph.D. thesis, University of Vienna, 2020.
- [10] Y. Y. Fein, A. Shayeghi, L. Mairhofer, F. Kiařka, P. Rieser, P. Geyer, S. Gerlich, and M. Arndt, Quantum-Assisted Measurement of Atomic Diamagnetism, *Phys. Rev. X* **10**, 011014 (2020).
- [11] S. Gerlich, Y. Y. Fein, A. Shayeghi, V. Köhler, M. Mayor, and M. Arndt, Otto Stern’s legacy in quantum optics: Matter waves and deflectometry, in *Molecular Beams in Physics and Chemistry: From Otto Stern’s Pioneering Exploits to Present-Day Feats*, edited by B. Friedrich and H. Schmidt-Böcking (Springer International Publishing, New York, 2021), pp. 547–573.
- [12] K. Hornberger, S. Gerlich, P. Haslinger, S. Nimmrichter, and M. Arndt, Colloquium: Quantum interference of clusters and molecules, *Rev. Mod. Phys.* **84**, 157 (2012).
- [13] J. F. Clauser and S. Li, Talbot-vonLau atom interferometry with cold slow potassium, *Phys. Rev. A* **49**, R2213 (1994).
- [14] J. Schmiedmayer, C. Ekstrom, M. Chapman, T. Hammond, and D. Pritchard, Magnetic coherences in atom interferometry, *J. Phys. II (France)* **4**, 2029 (1994).
- [15] M. Jacquy, A. Miffre, M. Büchner, G. Tréneç, and J. Vigué, Test of the isotopic and velocity selectivity of a lithium atom interferometer by magnetic dephasing, *Europhys. Lett.* **77**, 20007 (2007).
- [16] J. Gillot, A. Gauguet, M. Büchner, and J. Vigué, Optical pumping of a lithium atomic beam for atom interferometry, *Eur. Phys. J. D* **67**, 263 (2013).
- [17] W. A. de Heer and V. V. Kresin, Electric and magnetic dipole moments of free nanoclusters, in *Handbook of Nanophysics: Clusters and Fullerenes*, edited by K. D. Sattler (CRC Press, Boca Raton, 2010).
- [18] S. N. Khanna and S. Linderoth, Magnetic Behavior of Clusters of Ferromagnetic Transition Metals, *Phys. Rev. Lett.* **67**, 742 (1991).
- [19] X. Xu, S. Yin, R. Moro, and W. A. de Heer, Magnetic Moments and Adiabatic Magnetization of Free Cobalt Clusters, *Phys. Rev. Lett.* **95**, 237209 (2005).
- [20] M. B. Knickelbein, Spin relaxation in isolated molecules and clusters: The interpretation of Stern-Gerlach experiments, *J. Chem. Phys.* **121**, 5281 (2004).
- [21] S. Gerlich, L. Hackermüller, K. Hornberger, A. Stibor, H. Ulbricht, M. Gring, F. Goldfarb, T. Savas, M. Müri, M. Mayor, and M. Arndt, A Kapitza-Dirac-Talbot-Lau interferometer for highly polarizable molecules, *Nat. Phys.* **3**, 711 (2008).

- [22] See Supplemental Material at <http://link.aps.org/supplemental/10.1103/PhysRevLett.129.123001> for details on the characterization and modeling of the gradient field regions, additional experimental and data analysis details, and computational details for the rotational magnetic moments, which includes Ref. [24–31].
- [23] E. Majorana, Atomi orientati in campo magnetico variabile, *Nuovo Cimento* **9**, 43 (1932).
- [24] K. Hornberger, S. Uttenthaler, B. Brezger, L. Hackermüller, M. Arndt, and A. Zeilinger, Collisional Decoherence Observed in Matter Wave Interferometry, *Phys. Rev. Lett.* **90**, 160401 (2003).
- [25] H. Uys, J. D. Perreault, and A. D. Cronin, Matter-Wave Decoherence due to a Gas Environment in an Atom Interferometer, *Phys. Rev. Lett.* **95**, 150403 (2005).
- [26] J. R. Cheeseman, G. W. Trucks, T. A. Keith, and M. J. Frisch, A comparison of models for calculating nuclear magnetic resonance shielding tensors, *J. Chem. Phys.* **104**, 5497 (1996).
- [27] J. Gauss, K. Ruud, and T. Helgaker, Perturbation dependent atomic orbitals for the calculation of spin rotation constants and rotational g tensors, *J. Chem. Phys.* **105**, 2804 (1996).
- [28] D. J. D. Wilson, C. E. Mohn, and T. Helgaker, The rotational g tensor as a benchmark for density-functional theory calculations of molecular magnetic properties, *J. Chem. Theory Comput.* **1**, 877 (2005).
- [29] R. A. Kendall, T. H. Dunning, and R. J. Harrison, Electron affinities of the first row atoms revisited. Systematic basis sets and wave functions, *J. Chem. Phys.* **96**, 6796 (1992).
- [30] P. Storey and C. Cohen-Tannoudji, The Feynman path integral approach to atomic interferometry. A tutorial, *J. Phys. II (France)* **4**, 1999 (1994).
- [31] T. Bergeman, G. Erez, and H. J. Metcalf, Magnetostatic trapping fields for neutral atoms, *Phys. Rev. A* **35**, 1535 (1987).
- [32] J. M. Camacho and V. Sosa, Alternative method to calculate the magnetic field of permanent magnets with azimuthal symmetry, *Rev. Mex. Fis. E* **59**, 8 (2013).
- [33] A. D. Cronin, J. Schmiedmayer, and D. E. Pritchard, Optics and interferometry with atoms and molecules, *Rev. Mod. Phys.* **81**, 1051 (2009).
- [34] S. Nimmrichter and K. Hornberger, Theory of near-field matter-wave interference beyond the eikonal approximation, *Phys. Rev. A* **78**, 023612 (2008).
- [35] L. Mairhofer, S. Eibenberger, A. Shayeghi, and M. Arndt, A quantum ruler for magnetic deflectometry, *Entropy* **20**, 516 (2018).
- [36] Y. Y. Fein, A. Shayeghi, F. Kiałka, P. Geyer, S. Gerlich, and M. Arndt, Quantum-assisted diamagnetic deflection of molecules, *Phys. Chem. Chem. Phys.* **22**, 14036 (2020).
- [37] W. H. Flygare, Magnetic interactions in molecules and an analysis of molecular electronic charge distribution from magnetic parameters, *Chem. Rev.* **74**, 653 (1974).
- [38] D. M. Cox, D. J. Trevor, R. L. Whetten, E. A. Rohlfing, and A. Kaldor, Magnetic behavior of free-iron and iron oxide clusters, *Phys. Rev. B* **32**, 7290 (1985).
- [39] W. A. de Heer, P. Milani, and A. Chatelain, Spin Relaxation in Small Free Iron Clusters, *Phys. Rev. Lett.* **65**, 488 (1990).
- [40] J. P. Bucher, D. C. Douglass, and L. A. Bloomfield, Magnetic Properties of Free Cobalt Clusters, *Phys. Rev. Lett.* **66**, 3052 (1991).
- [41] The Langevin function, which describes the magnetization of a paramagnet in thermal equilibrium (for large angular momentum), is defined as $\mathcal{L}(x) = \coth(x) - 1/x$, with $x = \mu B/k_B T$.
- [42] F. W. Payne, W. Jiang, J. W. Emmert, J. Deng, and L. A. Bloomfield, Magnetic structure of free cobalt clusters studied with Stern-Gerlach deflection experiments, *Phys. Rev. B* **75**, 094431 (2007).
- [43] M. B. Knickelbein, Experimental Observation of Superparamagnetism in Manganese Clusters, *Phys. Rev. Lett.* **86**, 5255 (2001).
- [44] X. Xu, S. Yin, R. Moro, and W. A. de Heer, Distribution of magnetization of a cold ferromagnetic cluster beam, *Phys. Rev. B* **78**, 054430 (2008).
- [45] U. Rohrmann and R. Schäfer, Stern-Gerlach Experiments on Mn@Sn₁₂: Identification of a Paramagnetic Superatom and Vibrationally Induced Spin Orientation, *Phys. Rev. Lett.* **111**, 133401 (2013).
- [46] A. Amirav and G. Navon, Intramolecular spin relaxation probed by Stern-Gerlach experiments, *Chem. Phys.* **82**, 253 (1983).
- [47] A. Gedanken, N. A. Kuebler, M. B. Robin, and D. R. Herrick, Stern-Gerlach deflection spectra of nitrogen oxide radicals, *J. Chem. Phys.* **90**, 3981 (1989).
- [48] U. Even, J. Jortner, D. Noy, N. Lavie, and C. Cossart-Magos, Cooling of large molecules below 1 K and He clusters formation, *J. Chem. Phys.* **112**, 8068 (2000).
- [49] A. Amirav, U. Even, and J. Jortner, Cooling of large and heavy molecules in seeded supersonic beams, *Chem. Phys.* **51**, 31 (1980).
- [50] R. C. Haddon, Magnetism of the carbon allotropes, *Nature (London)* **378**, 249 (1995).
- [51] Y.-H. Kim, J. Choi, K. J. Chang, and D. Tománek, Defective fullerenes and nanotubes as molecular magnets: An *ab initio* study, *Phys. Rev. B* **68**, 125420 (2003).
- [52] J. R. Eshbach and M. W. P. Strandberg, Rotational magnetic moments of ¹Σ molecules, *Phys. Rev.* **85**, 24 (1952).
- [53] A. D. Becke, Density functional thermochemistry. III. The role of exact exchange, *J. Chem. Phys.* **98**, 5648 (1993).
- [54] F. Weigend and R. Ahlrichs, Balanced basis sets of split valence, triple zeta valence and quadruple zeta valence quality for H to Rn: Design and assessment of accuracy, *Phys. Chem. Chem. Phys.* **7**, 3297 (2005).
- [55] M. J. Frisch *et al.*, GAUSSIAN 16 revision C.01, Gaussian, Inc., 2016.
- [56] The J distribution is proportional to the product of the degeneracy and the Boltzmann factors. The degeneracy of spherical top molecules like C₆₀ is $(2J + 1)^2$ rather than $2J + 1$ as for symmetric tops.
- [57] Averaging over the J distribution at 870 K gives comparable results to using J_{\max} , which is computationally more efficient.
- [58] Rotational moments similarly do not play a strong role for TEMPO, especially given the low rotational temperatures produced in the supersonic expansion.